

Article

Investigation of Stresses Induced Due to the Mismatch of the Coefficients of Thermal Expansion of the Matrix and the Strengthening Particle in Aluminum-Based Composites

Oleg Matvienko ^{1,2}, Olga Daneyko ^{1,2}, Tatiana Kovalevskaya ^{1,2}, Anton Khrustalyov ^{1,*}, Ilya Zhukov ¹ and Alexander Vorozhtsov ¹

¹ Faculty of Physics and Engineering, National Research Tomsk State University, 634050 Tomsk, Russia; matvologv@mail.ru (O.M.); olya_dan@mail.ru (O.D.); takov47@mail.ru (T.K.); gofra930@gmail.com (I.Z.); abv@mail.tomsknet.ru (A.V.)

² Department of Physics, Chemistry and Theoretical Mechanics, Tomsk State University of Architecture and Building, 634003 Tomsk, Russia

* Correspondence: tofik0014@gmail.com; Tel.: +7-952-1555-568

Abstract: An experimental and theoretical investigation of the strength properties of aluminum alloys strengthened by dispersed nanoparticles, as well as the determination of the significance of various mechanisms responsible for the strengthening of the material, was carried out. Results of experimental investigation demonstrate that the hardening of aluminum alloy A356 by Al₂O₃ and ScF₃ nanoparticles leads to an increase in the yield strength, ultimate tensile strength, and plasticity. Despite the similar size of Al₂O₃ and ScF₃ nanoparticles, the physicomaterial properties of nanoparticles significantly affect the possibility of increasing the mechanical properties of the A356 aluminum alloy. A physicomathematical model of the occurrence of thermal stresses was developed caused by the mismatch of the coefficients of thermal expansion (CTEs) of the matrix and strengthening particles on the basis of the fundamental principles of mechanics of a deformable solid and taking into account the elastic properties of not only the matrix, but also the particle. The forming of thermal stresses induced due to the mismatch of the coefficients of thermal expansion of the matrix and the strengthening particle in aluminum-based composites was investigated. In the case of thermal deformation of dispersion-hardened alloys, when the CTE of the matrix and particles noticeably differ, an additional stress field is created in the vicinity of the strengthening particle. Thermal stresses increase the effective particle size. This phenomenon can significantly affect the result of the assessment of the yield strength. The strengthening caused by thermal mismatch makes the largest contribution to the yield strength improvement. The yield strength increments due to Nardoni–Prewett and Orowan mechanisms are much lower.

Keywords: deformation; dispersion-hardening; nanoparticles; stress; strain; plastic deformation; thermal stresses; aluminum



Citation: Matvienko, O.; Daneyko, O.; Kovalevskaya, T.; Khrustalyov, A.; Zhukov, I.; Vorozhtsov, A. Investigation of Stresses Induced Due to the Mismatch of the Coefficients of Thermal Expansion of the Matrix and the Strengthening Particle in Aluminum-Based Composites. *Metals* **2021**, *11*, 279. <https://doi.org/10.3390/met11020279>

Received: 9 December 2020

Accepted: 29 December 2020

Published: 5 February 2021

Publisher's Note: MDPI stays neutral with regard to jurisdictional claims in published maps and institutional affiliations.



Copyright: © 2021 by the authors. Licensee MDPI, Basel, Switzerland. This article is an open access article distributed under the terms and conditions of the Creative Commons Attribution (CC BY) license (<https://creativecommons.org/licenses/by/4.0/>).

1. Introduction

Aluminum-based alloys are widely used in the automobile industry not only because they are easily castable in complex forms but also because of their excellent wear resistance, light weight, and good strength, which make them widely used in the manufacture of numerous automotive parts, such as engine blocks and wheels. Additionally, aluminum-based alloys are used as a matrix for obtaining composites [1,2], which have an enhanced wear resistance, favorable mechanical properties, and higher strength, Young's modulus, and fatigue resistance [3,4] at room and elevated temperatures. Dispersion-hardened alloys are characterized by isotropic mechanical properties, high plasticity, and high strength [5,6]. The physical theory of plasticity and strain hardening was developed by Orowan [7], Ashby [8], Hirsch, and Humphreys [9,10].

According to continuum linear elastic dislocation theory, Orowan [7] proposed that the interaction between dislocation and hardening particles leads to the formation of shear loops around the particles. This dislocation interaction scenario leads to what is known as Orowan strain hardening. Humphreys and Hirsch [11] proposed an alternative mechanism in which, if all dislocations are edge-oriented, each dislocation/particle interaction leads to two pairs of prismatic loops, one on each side of the particle. This multi-dislocation interaction, which involves the cross-slip of screw components of dislocations, is known as Hirsch looping. The material hardening depends on the types of particles, their volume fraction and homogeneous distribution in the matrix, and the interaction between matrix and strengthening particles.

The stress–strain curves at room temperature and at 400 °C for various types of dispersion-hardened aluminum alloys were determined in [12]. The results of investigations demonstrated that the effect of particles on the flow stress is in agreement with Orowan’s theory [7]. A model to describe the creep of FCC metals has been used [13] for alloys and composites strengthened by the dispersion of nanosized particles. According to investigation results, the volume fraction and size of the nanosized particulate assumes a key role in determining the creep response of these materials. The results of investigations of the mechanical properties of aluminum alloys indicate that the hardness, yield strength, and ultimate tensile strength of the Al–2 vol.% C₆₀ nanocomposites are higher than those of the monolithic Al samples.

The investigation in [14] dealt with aspects of the deformation behavior of dispersion-hardened aluminum materials during uniaxial creep in a broad temperature range. Results of the investigation demonstrated that the threshold stress decreases considerably with increasing temperature.

The authors of [15] focused on the examination of materials of submicron matrix grain size strengthened with nanosized particles. The results obtained within the scope of this work showed the possibility for significant improvement of the microcomposite properties.

The results of the studies of the effect of nanodiamond addition on the physico-mechanical properties of the drilling tool metal matrix were discussed in [16]. The optimal concentration of nanodiamond powder additives in the composition of a hard alloy mixture was defined. The addition of 1–2 wt.% nanodispersed diamonds was shown to contribute to binding oxygen in the thermo-oxidation of diamond in the course of the tool manufacture, which makes it possible to reduce the number of pores in the matrix material structure and to increase its density by 1.7% and hardness by 24.3%.

In [17], the effect of the aspect ratio of carbon nanotubes (CNTs) on strengthening aluminum metal matrix composites (Al MMCs) was investigated. The tensile results showed that the CNTs exhibited a strong strengthening effect in the composites regardless of their aspect ratios. However, the post-loading examination and quantitative analysis indicated that there was a strengthening mechanism transition for CNTs, which was closely associated with the aspect ratio or length of CNTs. The origin of such a transition was explored from the viewpoint of the dislocation–CNT interaction under loading.

The effect of Al₄C₃ formation on the tensile properties of multiwalled carbon nanotubes which reinforce an Al metal matrix was investigated in [18]. It was concluded that the formation of Al₄C₃ could effectively enhance the load transfer in composites.

Mathematical modeling of composites hardened by nanoparticles with a metal matrix was considered in [19]. The authors covered in detail the effect of the bulk content, distribution, and morphology of nanoparticles per average path length of a dislocation in the alloy (L). The authors revealed that the uniform distribution of grains in the matrix gave the smallest value of L. An increase in the bulk content of nanoparticles from 1 to 7 vol.% decreased the average path length of the dislocation by 50%, and, if their fraction exceeded 7 vol.%, the value of L was almost invariable.

In [20–23], a physical model of plastic deformation was suggested. The modeling of plastic deformation and strain hardening is based on the concept that the plastic slip in FCC alloys with incoherent nanoparticles leads to the formation of a defect structure with

shear-forming dislocations, prismatic dislocation loops of vacancy and interstitial types, dislocation dipoles of vacancy and interstitial types, and interstitial atoms, monovacancies, and bivacancies.

An approach which combines methods of plasticity physics and mechanics of deformable solid was used in [24–26] to explore the limits of elastic and plastic resistance of the tube from dispersion-hardened aluminum alloy subjected to internal and external pressure.

It is known that, in composites, there is a large difference in the coefficients of thermal expansion between the matrix and the strengthening particles [27–29]. Thermally induced stresses could be generated as the result of a global heating and cooling of constructions, as well as local heating and cooling effects when a temperature gradient develops.

Therefore, the problem of thermally induced stresses due to a mismatch of the coefficients of thermal expansion between the matrix and strengthening particles has implications for the determination of mechanical properties of composite materials. The stress–strain state in plastic area around an oversized spherical particle which was introduced into a spherical hole in the matrix was analyzed in [30]. The analysis of stress–strain state must consider the contribution of thermally induced stresses in addition to the mechanically induced stresses [31]. These thermal stresses may be higher than the yield strength of the matrix and induce either debonding between particles and matrix or crack propagation leading to damage accumulation in the matrix [32,33].

The thermal stresses may be sufficient to generate new dislocations at the interfaces between the matrix and the reinforcement. In [29,34], the authors proposed that the increased strength observed in Al–SiC composites could be accounted for by a high dislocation density in the aluminum matrix, as observed in transmission electron microscopy (TEM). An increase in the density of newly created dislocations near reinforcement fibers was calculated in [24,35]. According to [36], when the composite is heated or cooled, misfit strains which are sufficient to generate dislocations occur because of differential thermal contraction at the Al–SiC interface. The investigations of the elastic and plastic stresses and strains generated about an inclusion, which has a coefficient of thermal expansion different from that of the matrix as a result of heating or cooling, was carried out in [34]. Furthermore, an in situ transmission electron microscopy investigation was undertaken into dislocation generation at the composite due to the differential thermal contraction. A simple model based on results of experimental investigation was developed to account for the relative dislocation density due to the differential thermal contraction.

Thus, it is very important to analyze the thermal stresses on the particle–matrix interface in order to predict a possible modification of the composite properties [37].

The purpose of this work was to experimentally and theoretically investigate the strength properties of aluminum alloys strengthened by nanoparticles, as well as to determine the significance of various mechanisms responsible for strengthening the material. Particular attention is paid to the development of a physicomathematical model of the occurrence of thermal stresses caused by a mismatch between the coefficients of thermal expansion (CTEs) of the matrix and strengthening particles, according to the fundamental principles of solid mechanics and taking into account, in contrast to previously existing models, the elastic properties of not only the matrix, but also the particle.

2. Methods

2.1. Experimental Procedure

As initial materials, we used nanopowders of ScF₃ (~80 nm), obtained via the sol–gel method [38], and alumina (~80 nm), obtained via the method of electric explosion of a conductor (EEW) [39], aluminum micropowder (<20 μm) [39], and A356 aluminum alloy. Figure 1 shows TEM images of the initial powders.

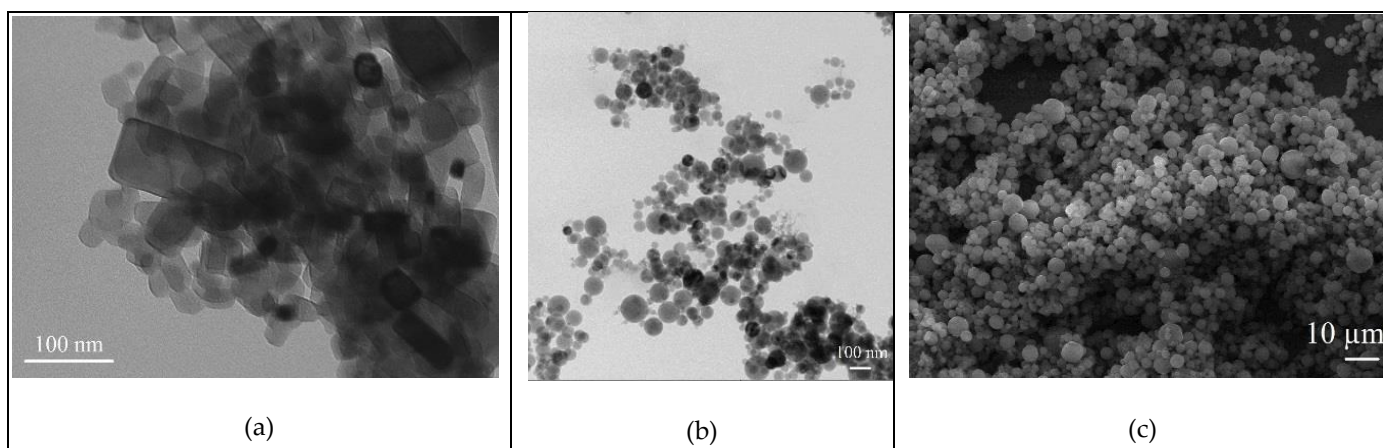


Figure 1. Transmission electron microscopy (TEM) images of initial powders: ScF₃ (a); Al₂O₃ (b); Al (c).

As initial components for the synthesis of ScF₃ nanoparticles, scandium oxide, hydrofluoric acid, and hydrochloric acid were used, which makes the process safer, without the use of poisonous fluorine, which is used in the direct synthesis of ScF₃ from metallic scandium.

For the introduction of nanoparticles, a powder mixture of Al–5 wt.% nanoparticles was prepared. For deagglomeration and distribution of nanoparticles in the powder mixture, stearic acid was used as a surfactant. First, 200 mL of petroleum ether and 1.5 wt.% stearic acid were added to the powder mixture. Then, for 20 min, the powder mixture was mechanically mixed. After mechanical mixing, the aluminum–nanoparticle powder mixture was air-dried (90 °C) and sieved. The resulting powder mixture was introduced into the melt using ultrasonic treatment, which allows degassing and refining the melt, preventing deagglomeration, and evenly distributing nanoparticles in the volume [40].

Aluminum alloy A356 was melted in a graphite crucible with a total melt volume of 500 g. Ultrasonic treatment was carried out using a water-cooled magnetostrictive transducer (power—5 kW, frequency—17.5 kHz, RELTECH, Saint-Petersburg, Russia). The waveguide of the ultrasonic equipment was made in the form of a niobium alloy (VN2AE) cone, the working amplitude of which was 30 μm. At a melt temperature of 730 °C, ultrasonic degassing was carried out for 1 min. After degassing, an aluminum–nanoparticle master alloy (5 wt.%) was introduced into the melt with ultrasonic treatment. After dissolution of the master alloy in the melt, ultrasonic treatment lasted for 2 min (temperature, 730 °C). The melt obtained at a temperature of 710 °C was poured into a steel chill mold. The amount of ScF₃ and Al₂O₃ nanoparticles in the A356 aluminum alloy ranged from 0 to 1 wt.%. The A356 alloy without particles was obtained with similar melt processing parameters. Mechanical tests were performed on a universal testing machine (Instron European Headquarters, High Wycombe, UK), Instron 3369, at a speed of 0.2 mm/min. The samples were tensioned at room temperature (25 °C), and the number of samples for each composition was at least four pieces. The structures of the obtained materials were investigated through optical microscopy, Olympus GX71 (Olympus Scientific Solutions Americas, Waltham, MA, USA). Samples were subjected to preliminary mechanical polishing, electrolytical etching, and anodization. The electrochemical oxidation of the metallographic specimen surface in a 5% solution of hydrofluoric acid (HBF₄) at a voltage of 20 V and a current of 2 A was carried out to identify grain boundaries.

2.2. Strengthening Mechanism

It is generally accepted that nanocomposite hardening occurs due to the load transfer, Orowan mechanism, and CTE mismatch mechanism [41]. The total strengthening can be calculated as a superposition of the individual strengthening mechanisms.

$$\sigma_Y = \sigma_{Ym} + \sigma_{NP} + \sigma_{HP} + \sigma_{Or} + \sigma_{CTE}, \quad (1)$$

where σ_{Ym} is the yield strength of the matrix, σ_{NP} is the stress caused by the transfer of the load from the matrix to the particles, σ_{Or} is the Orowan stress, σ_{CTE} is the thermal stress arising from the difference in the coefficients of thermal expansion, elastic modulus, and shear modulus of the matrix and the particle.

The load transfer mechanism is the most accepted strengthening mechanism. The transfer of the load from the soft matrix to the hard particles when an external load is applied helps to harden the material, as proposed by Nardon and Prewo [42].

$$\sigma_{NP} = 0.5f_p\sigma_{Ym}, \quad (2)$$

where f_p is the volume fraction of particles.

The grain size has an influence on the strength of the alloy, since the grain boundaries can impede the movement of dislocations. This is due to the different orientations of adjacent grains and to the high lattice disorder characteristic of these regions, which prevents the glide of dislocations in a continuous slip plane. The Hall–Petch equation relates stress to average grain size. There are empirical models available for predicting the yield strength change due to the change in the grain size in metal matrix composites by extending the Hall–Petch [43,44] relationship as follows:

$$\sigma_{HP} = k_Y \left(\frac{1}{\sqrt{d_{gr}}} - \frac{1}{\sqrt{d_{gr0}}} \right), \quad (3)$$

where σ_{HP} is the change in tensile strength due to the contribution of the Hall–Petch law, k_Y is the hardening coefficient (constant for each material), and d_{gr} and d_{gr0} are the average grain sizes of the obtained alloys. This equation assumes that the Hall–Petch parameters $k_Y \approx 68 \text{ MPa}\cdot(\mu\text{m})^{1/2}$ for Al alloys [45].

Particles perform a fundamental role in the final grain size of the matrix of composites as they can interact with grain boundaries and act as nuclei of crystallization, slowing or stopping grain growth. An increase in the volume fraction f_p and a decrease in the particle diameter δ_p lead to a finer-grained structure, which is theoretically modeled by the Zener–Smith equation [46].

$$d_{gr} = k_z \frac{\delta}{f_p}, \quad (4)$$

where k_z coefficient values are in the range $0.1 < k_z < 1$. Equation (5) is theoretically derived to describe the deceleration of migrating grain boundaries by particles.

The Orowan mechanism is based on the interaction of nanoparticles with dislocations. Solid “noncutting” particles impede the movement of dislocations, which leads to bending of the dislocation line around the particles (Orowan loops) under the action of an external load [47]. The Orowan mechanism is very important in metal matrix composites, hardening by fine particles when the interparticle distance is not large. An increase in the composite yield strength by Orowan stress may be expressed as follows [47]:

$$\sigma_{Or} = G_m \frac{b}{\Lambda_p - 2R_p}, \quad (5)$$

where G_m is the matrix shear modulus, b is the Burgers vector of the matrix ($b = 0.202 \text{ nm}$), and Λ_p is the distance between particles.

When a composite is subjected to heating or cooling, the difference in the coefficients of thermal expansion, elastic modulus, and shear modulus between the matrix and hardening particles produce internal stress state changes. The improvement in yield strength from thermal mismatch can be calculated using the equation suggested in [48–50].

$$\sigma_{CTE} = 6G_m \sqrt{(\alpha_m - \alpha_p)\Delta T \frac{b}{\delta_p} \frac{f_p}{1 - f_p}}. \quad (6)$$

Equation (6) was obtained on the basis of the simplest geometric estimates under the assumption that the volume mismatch between the matrix and the reinforcing particles, arising from the difference in thermal expansion coefficients, leads to the appearance of geometrically necessary dislocations around the reinforcing particles. The disadvantages of the above approach include the fact that the stresses in Equation (6) do not depend on the elastic properties of the strengthening particles.

A more rigorous assessment of the thermal stresses arising from the difference in the coefficients of thermal expansion, elastic modulus, and shear modulus of the matrix and particle can be carried out using the methods of solid mechanics.

2.3. Mathematical Model of the Stresses Caused by the Thermal Expansion Mismatch between the Matrix and Strengthening Particles

Let us consider the stress–strain state that arises as a result of a change in the temperature of a spherical particle with a radius R_p surrounded by a matrix. The coefficients of linear thermal expansion of materials are assumed to be different.

The equation of equilibrium of an elastic medium in spherical coordinates under the assumption of spherical symmetry can be written in the following form:

$$\frac{\partial \sigma_{rr}}{\partial r} + \frac{2\sigma_{rr} - \sigma_{\varphi\varphi} - \sigma_{\theta\theta}}{r} = 0 \quad (7)$$

The relationship between stresses σ_{ij} and strains ε_{ij} , expressing the generalized Hooke's law, under nonisothermal conditions, according to the von Neumann hypothesis, has the following form:

$$\sigma_{ij} = \lambda \varepsilon_{kk} \delta_{ij} + 2G\varepsilon_{ij} - 3K\alpha\Delta T\delta_{ij}, \quad (8)$$

where λ is the the Lamé coefficient, G is the shear modulus, K is the bulk strain modulus, α is the coefficient of linear thermal expansion, $\Delta T = T_{\text{test}} - T_{\text{room}}$ is the temperature difference between the testing temperature T_{test} and room temperature T_{room} , and δ_{ij} is the Kronecker symbol.

The components of the strain tensor under spherical symmetry are

$$\varepsilon_{rr} = \frac{\partial u}{\partial r}, \quad \varepsilon_{\varphi\varphi} = \frac{u}{r}, \quad \varepsilon_{\theta\theta} = \frac{u}{r}, \quad \varepsilon_{r\varphi} = 0, \quad \varepsilon_{r\theta} = 0, \quad \varepsilon_{\varphi\theta} = 0. \quad (9)$$

Substituting into the equilibrium equation stresses expressed in terms of displacements, we obtain

$$\frac{\partial}{\partial r} \left[\frac{1}{r^2} \frac{\partial}{\partial r} (ur^2) \right] = 0. \quad (10)$$

First, we integrate Equation (11) for a spherical particle for the following boundary conditions:

$$r = 0: \quad u = 0; \quad r = R_p: \quad u = U. \quad (11)$$

As a result of simple calculations, we obtain the displacement field in the particle.

$$u = U \frac{r}{R_p}. \quad (12)$$

The stress field in a particle using the generalized Hooke's law has the following form:

$$\sigma_{rr} = (3\lambda_p + 2G_p) \frac{U}{R_p} - 3K_p\alpha_p\Delta T, \quad (13)$$

$$\sigma_{\varphi\varphi} = (3\lambda_p + 2G_p) \frac{U}{R_p} - 3K_p\alpha_p\Delta T, \quad (14)$$

$$\sigma_{\theta\theta} = (3\lambda_p + 2G_p) \frac{U}{R_p} - 3K_p\alpha_p\Delta T. \quad (15)$$

The displacement of the matrix material can be defined as

$$u = \alpha_m \Delta T r + \frac{UR_p^2 - \alpha_m \Delta T R_p^3}{r^2}. \quad (16)$$

The parameter U is determined from the condition of continuity of the radial stresses at the boundary between the particle and the matrix: $\sigma_{rr}|_- = \sigma_{rr}|_+$. As a result, we obtain

$$U = \frac{3K_p \alpha_p + 4G_m \alpha_m}{3K_p + 4G_m} \Delta T R_p. \quad (17)$$

Using the generalized Hooke's law, one can determine the stress field in the matrix.

$$\sigma_{rr} = -12 \frac{K_p G_m}{3K_p + 4G_m} (\alpha_p - \alpha_m) \Delta T \frac{R_p^3}{r^3}, \quad (18)$$

$$\sigma_{\varphi\varphi} = 6 \frac{K_p G_m}{3K_p + 4G_m} (\alpha_p - \alpha_m) \Delta T \frac{R_p^3}{r^3}, \quad (19)$$

$$\sigma_{\theta\theta} = 6 \frac{K_p G_m}{3K_p + 4G_m} (\alpha_p - \alpha_m) \Delta T \frac{R_p^3}{r^3}. \quad (20)$$

We now turn from considering the stresses created by a single particle to the stresses caused by an ensemble of particles. The stress intensity characterizing the stress state of the material is determined by the following equation:

$$\sigma_{\text{int}} = \sqrt{\frac{1}{2} (\sigma_{rr}^2 + \sigma_{\varphi\varphi}^2 + \sigma_{\theta\theta}^2 - 3(\sigma_{rr} + \sigma_{\varphi\varphi} + \sigma_{\theta\theta})^2)}. \quad (21)$$

Taking into account Equations (13)–(15) and (18)–(20), the intensity of stresses caused by the difference in the coefficients of thermal expansion of the strengthening particles and the matrix is equal to

$$\sigma_{\text{int}} = 6\sqrt{3} \frac{K_p G_m}{3K_p + 4G_m} |\alpha_p - \alpha_m| \Delta T \min \left[1, \frac{R_p^3}{r^3} \right]. \quad (22)$$

The average value of the thermal stress arising from the difference in the coefficients of thermal expansion, elastic modulus, and shear modulus of the matrix and the particle is determined using the traditional procedure of averaging over a spherical volume with a radius $\Lambda_p/2$.

$$\sigma_{\text{CTE}} = \frac{24}{\Lambda_p^3} \int_0^{\Lambda_p/2} \sigma_{\text{int}} r^2 dr. \quad (23)$$

Thus, the average value of thermal stresses can be estimated as

$$\sigma_{\text{CTE}} = 6\sqrt{3} \frac{K_p G_m}{3K_p + 4G_m} f_p |\alpha_p - \alpha_m| \Delta T (1 - \ln f_p). \quad (24)$$

3. Results and Discussion

3.1. Experimental Results

Figure 2 shows SEM images of the microstructure of A356 aluminum alloys. The structure of the initial A356 alloy does not differ significantly from the alloys with ScF₃ nanoparticles. Silicon inclusions are present in the structure of all alloys (Figure 2a,b). At the same time, ScF₃ nanoparticles are concentrated in the A356 aluminum alloy around the silicon inclusions (Figure 2c,d) and along the grain boundaries. The nonregular distribution of nanoparticles in the structure of the A356 alloy occurs due to the force of attraction

between nanosized inclusions, as well as under the influence of the solidification front, which displaces them to the boundaries when the melt is cooled.

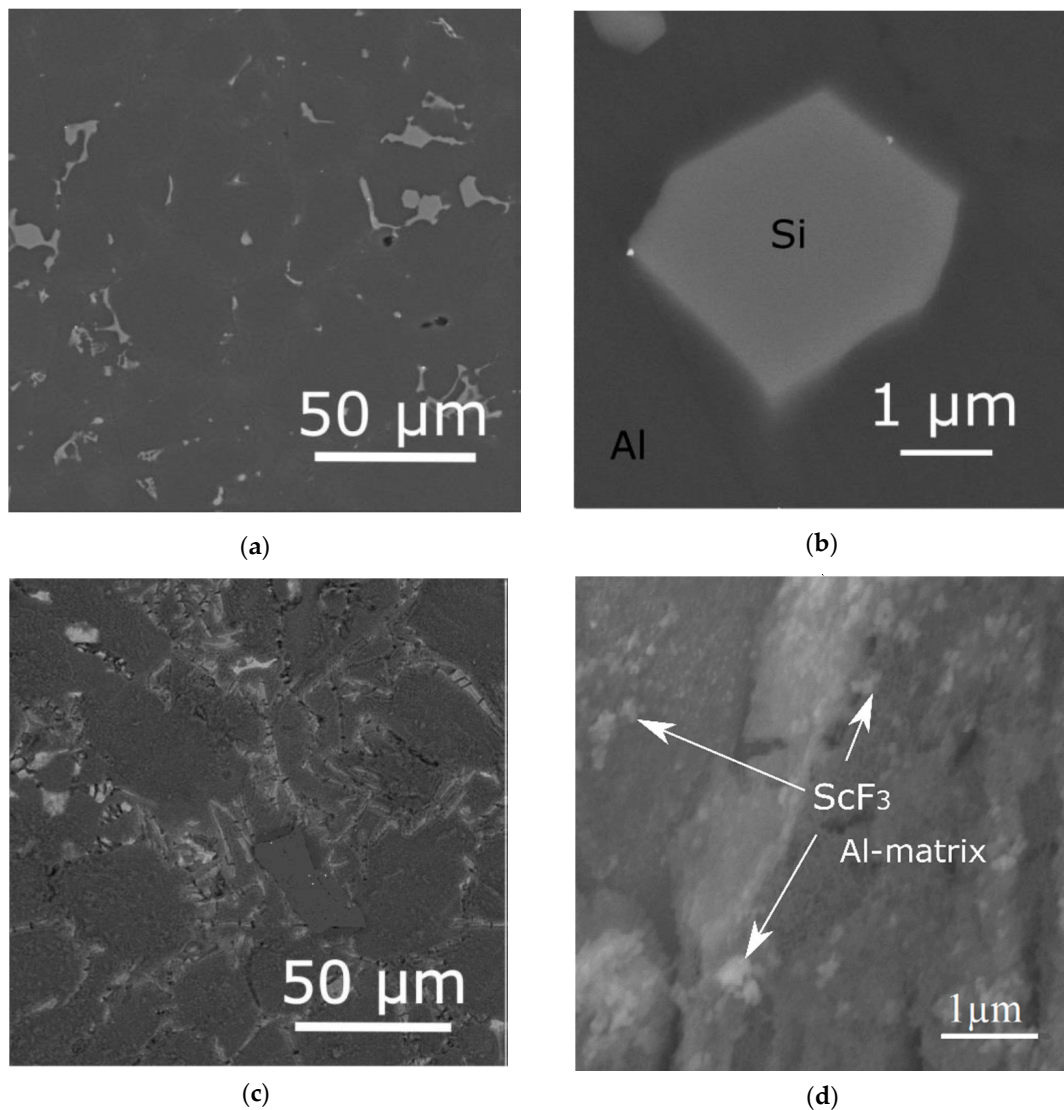


Figure 2. SEM images of the structure A356 alloys (a,b) and A356–1% ScF₃ (c,d).

The microstructures of the initial aluminum alloy A356, A356 + 0.2% ScF₃, and A356 + 1% ScF₃ are shown in Figure 3. It can be seen that the introduction of 0.2% ScF₃ nanoparticles into the aluminum alloy led to a decrease in the average grain size from 310 to 190 μm. An increase in the amount of nanoparticles in the A356 alloy to 1% led to a decrease in the grain size to 100 μm.

Figure 4 shows tensile diagrams, and Table 1 shows data on the mechanical properties of aluminum alloys strengthened with ScF₃ and Al₂O₃ nanoparticles. The results were obtained at room temperature ($T_{\text{room}} = 293$ K).

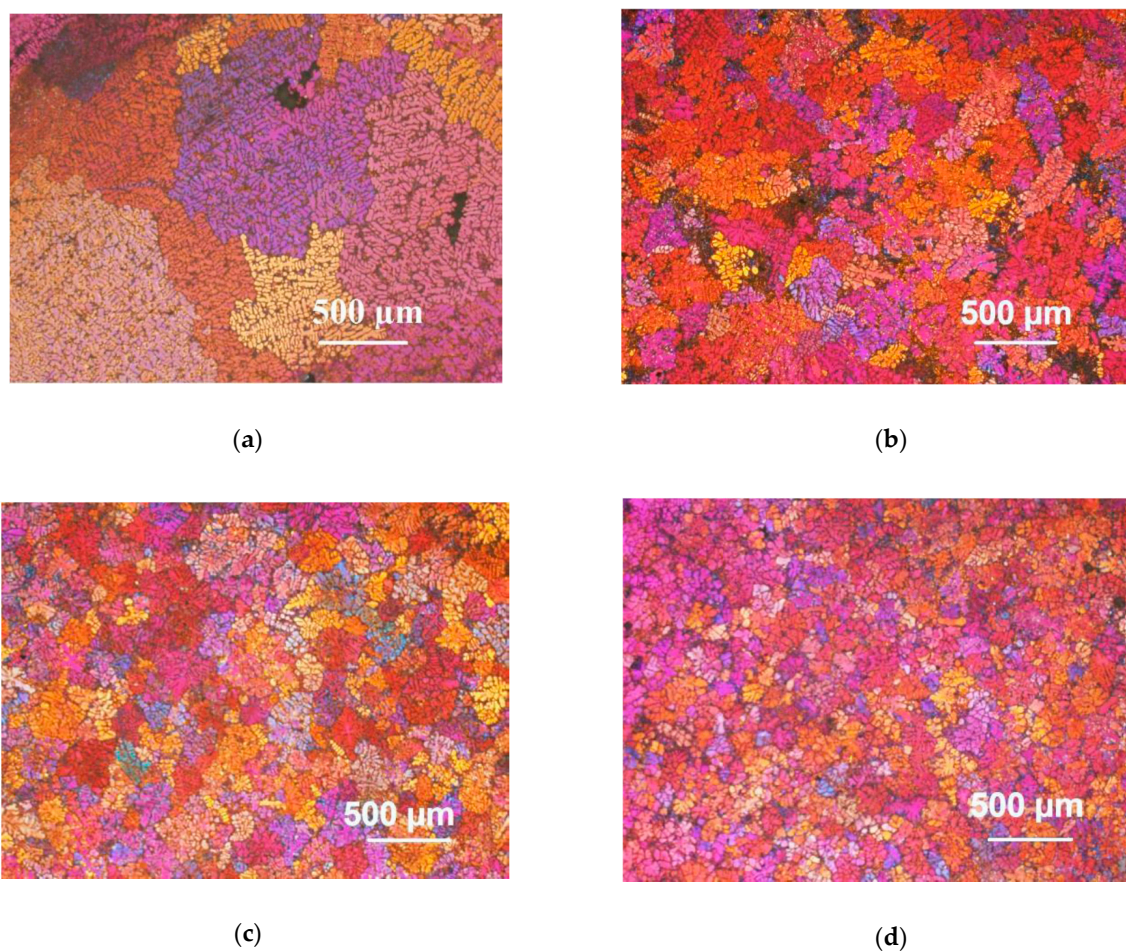


Figure 3. Microstructure of A356 alloy without treatment (a), A356 after ultrasonic treatment (b), A356–0.2% ScF₃ (c), and A356–1% ScF₃ (d).

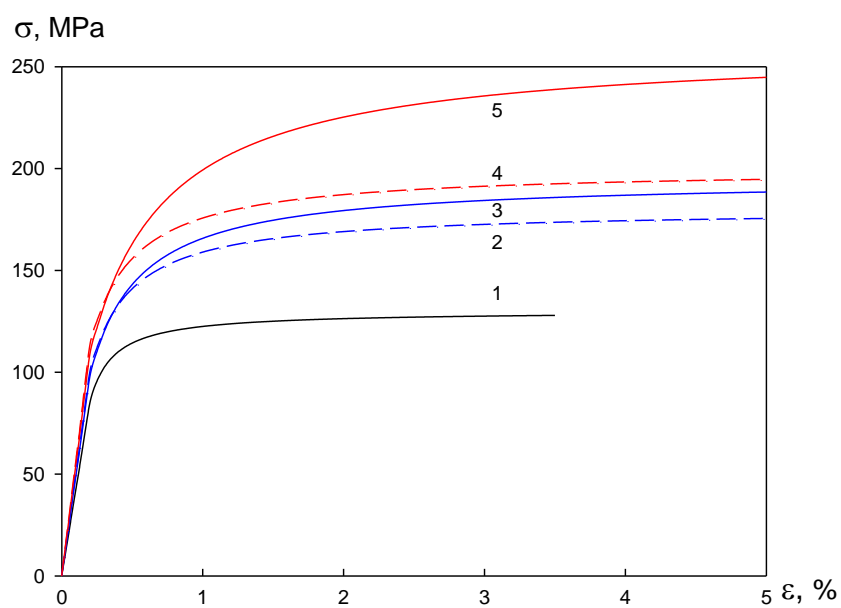


Figure 4. Loading diagrams of aluminum alloys: 1—A356; 2—A356–0.2% Al₂O₃; 3—A356–0.2% ScF₃; 4—A356–1% Al₂O₃; 5—A356–1% ScF₃.

Table 1. Mechanical properties of aluminum alloys.

Alloy	$\sigma_{0.2}$ (MPa)	σ_B (MPa)	Plasticity (%)
A356	85 ± 8	130 ± 7	3.5 ± 0.1
A356–0.2% ScF ₃	98 ± 6	190 ± 11	4.3 ± 0.3
A356–1% ScF ₃	109 ± 8	250 ± 9	4.2 ± 0.1
A356–0.2% Al ₂ O ₃	100 ± 4	180 ± 7	4.4 ± 0.2
A356–1% Al ₂ O ₃	113 ± 6	195 ± 4	4.1 ± 0.3

Figure 4 and Table 1 demonstrate that the hardening of aluminum alloy A356 by Al₂O₃ and ScF₃ nanoparticles led to an increase in the yield strength, ultimate tensile strength, and plasticity. The introduction of 0.2 wt.% Al₂O₃ nanoparticles made it possible to increase the yield strength, ultimate tensile strength, and plasticity from 85 to 100 MPa, from 130 to 180 MPa, and from 3.5% to 4.1%, respectively, and an increase in the content of Al₂O₃ nanoparticles allowed an increase in the yield strength and ultimate tensile strength of the alloy to 113 MPa and 195 MPa, respectively.

The use of 0.2 wt.% ScF₃ nanoparticles increased the yield strength, ultimate tensile strength, and ductility of the A356 aluminum alloy to 98, 190 MPa, and 4.3%, respectively, and an increase in the content of ScF₃ nanoparticles made it possible to increase the yield strength and ultimate tensile strength of the alloy to 109 MPa and 250 MPa, respectively. Despite the similar size of Al₂O₃ and ScF₃ nanoparticles (~80 nm), the physicomaterial properties of nanoparticles significantly affected the possibility of increasing the mechanical properties of the A356 aluminum alloy.

The approximation of the obtained experimental stress–strain curve allowed us to obtain the function of $\sigma(\varepsilon)$ with an error not exceeding 0.1%.

$$\sigma = \begin{cases} G\varepsilon, & \text{if } \varepsilon \leq \tau_0/G \\ \tau_0 + \tau_1 \frac{\varepsilon - \tau_0/G}{\varepsilon_* + \varepsilon}, & \text{if } \tau_0/G < \varepsilon \end{cases} \quad (25)$$

where τ_0 is the yield strength, $\tau_1 = \tau_\infty - \tau_0$ is the hardening stress, which characterizes the maximum increase of the flow stress during the plastic deformation, and ε_* is an empirical parameter that determines the rate at which the flow curve reaches the asymptote.

The values of the material constants: τ_{0*} , τ_{1*} , and ε_* for various volume fractions of scandium fluoride particles are presented in Table 2.

Table 2. The material constants τ_{0*} , τ_{1*} , and ε_* .

Alloy	τ_{0*} (MPa)	τ_{1*} (MPa)	ε_*
A356–0.2% ScF ₃	98	92	0.011
A356–1% ScF ₃	109	141	0.013
A356–0.2% Al ₂ O ₃	102	78	0.012
A356–1% Al ₂ O ₃	114	81	0.013

3.2. Results of Theoretical Investigation

The theoretical investigations were conducted for a matrix of aluminum Al 5083 alloy hardened by reinforcement particles. The main calculations were performed for the following parameters [51]: $\alpha_m = 2.3 \times 10^{-5} \text{ K}^{-1}$, Young modulus of 73 GPa, matrix shear modulus of $G_m = 28.08 \text{ GPa}$, and yield strength of $\sigma_{Ym} = 85 \text{ MPa}$.

A variety of oxides, carbides, borides, and fluorides were utilized as the reinforcement phase in aluminum alloys. Some selected physical and mechanical properties of commonly used reinforcements are summarized in Table 3.

Table 3. Characteristics of reinforcement particles.

Reinforcement	Density (g/cm ³)	Young Modulus (GPa)	Shear Modulus (GPa)	Coefficient Thermal Expansion (10 ⁻⁶ K)
SiC	3.15–3.20	450–480	90–131	3.9–4.3
B ₄ C	2.35–2.55	440–472	180–195	3.2–3.4
ScF ₃	2.51–2.54	98–101	37–39	−(1.4–1.2)
TiB ₂	4.43–4.52	500–545	182–191	4.6–4.7
Al ₂ O ₃	3.94–3.96	450–460	88–162	7.7–8.5
TiO ₂	3.97–4.05	276–288	108–114	8.4–11.8

Let us consider the contribution of various mechanisms to material hardening.

The intensity of the stresses caused by the transfer of the load from the matrix to the particles σ_{NP} is determined by the volume fraction of the hardening particles and, at $f_p = 0.01$, is 0.5% of the yield strength of the matrix material. For $\sigma_{Ym} = 85$ MPa, the calculated value of $\sigma_{NP} = 0.425$ MPa, which indicates an insignificant contribution of this mechanism to the hardening of the material.

The influence of the average grain size on the stress intensity is rated by the Hall–Petch law, which describes the hardening of a material through the retardation of dislocations by grain boundaries in a polycrystal. The values were calculated (Equation (4)) taking into account the average grain size d_{gr} obtained from optical images of the structure (Figure 3). The calculated values σ_{HP} for the alloys were as follows: A356—2.5 MPa, A356–0.2%—3.2 MPa, and A356–1%—3.7 MPa. Despite a significant decrease in the average grain size, this mechanism had little effect on the increase in the mechanical properties of the A356 alloy. Taking this into account, the effect of the difference in CTE should be considered.

Let us proceed to the analysis of the effect of Orowan stress on the material hardening process. For convenience of analysis, we rewrite Equation (5) in the following form:

$$\sigma_{Or} = G_m \frac{b}{\Lambda_p - 2R_p} = G_m \frac{b}{\delta_p} \frac{\sqrt[3]{f_p}}{1 - \sqrt[3]{f_p}}. \quad (26)$$

Figure 5 shows the dependence of Orowan stresses on the volume fraction of hardening particles, calculated according to Equation (26).

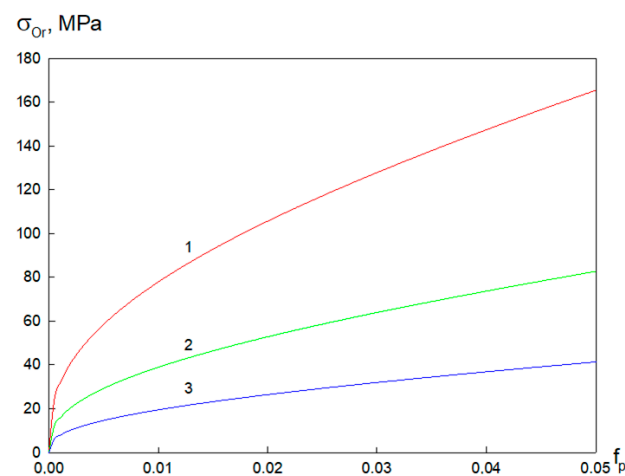


Figure 5. Dependence of Orowan stresses σ_{Or} in alloy A356 strengthened by ScF₃ particles on the volume fraction of hardening particles, calculated for $\Delta T = 100$ K. Particle size: 1— $\delta_p = 20$ nm; 2— $\delta_p = 40$ nm; 3— $\delta_p = 80$ nm.

It can be seen from Figure 5 that an increase in the volume fraction of hardening particles at the same size led to an increase in Orowan stresses. A similar effect was observed with an increase in the size of particles at the same volume fraction. This effect was associated with a decrease in the minimum distance between particles $\Lambda_p - \delta_p$. Dislocations under the influence of the applied external influence bypass the particles, leaving rings around them (“Orowan rings”). If this process occurs when the amount of bend is small, then the required increase in energy will be less than in the case when the dislocation line must completely loop around the particles before it is released. As the distance between the particles decreases, the length of the dislocation line increases significantly. As a result, the efficiency of particles as obstacles to the movement of dislocations increases, and the Orowan stresses increase.

Let us proceed to the analysis of the effect of thermal stresses arising from the difference in the coefficients of thermal expansion, elastic modulus, and shear modulus of the matrix and the particle on the hardening of the material.

In Figure 6, the dependence of the radial stresses σ_{rr} in the particle and matrix on the radial coordinate is shown when the composite was heated from room temperature (293 K). A region of tensile stresses is formed due to the difference in elastic properties. The radial stresses in the particle material have constant values. In the matrix material, these stresses decrease quite sharply with increasing distance from the particle and matrix interface and become negligible at a distance on the order of $5R_p$.

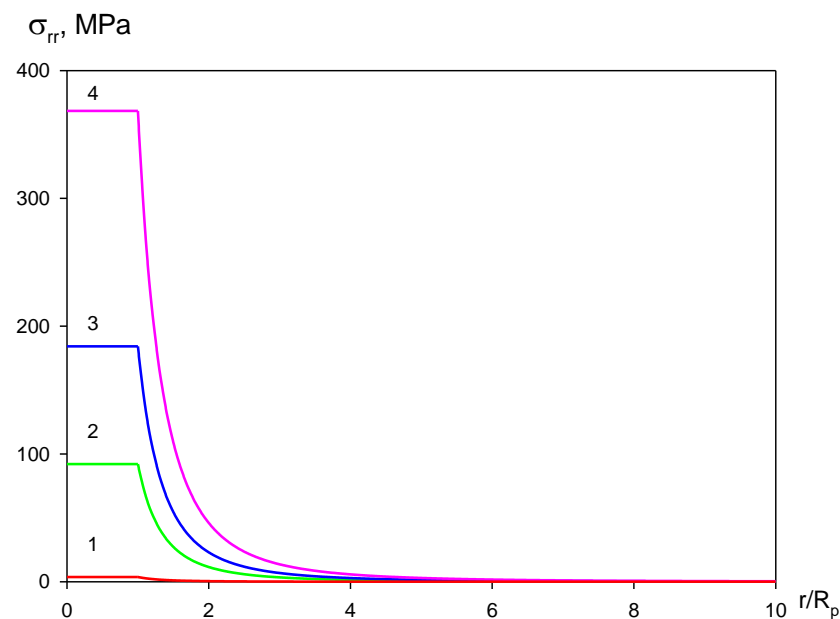


Figure 6. The distribution of the radial stresses σ_{rr} in the particle ScF_3 and matrix for various values of the temperature difference: 1— $\Delta T = 10$ K; 2—50 K; 3—100 K; 4—200 K.

Figure 7 shows the radial distribution of tangential stresses when the composite was heated from room temperature (293 K). In a particle, these stresses have constant positive values, which are associated with stretching due to the impact of the matrix. A sharp jump in tangential stress occurs at the boundary between the particle and the matrix. In this case, tangential stresses become compressive. The tangential stresses decrease sharply with an increase in the distance from the interface and become negligible at a distance on the order of $5R_p$.

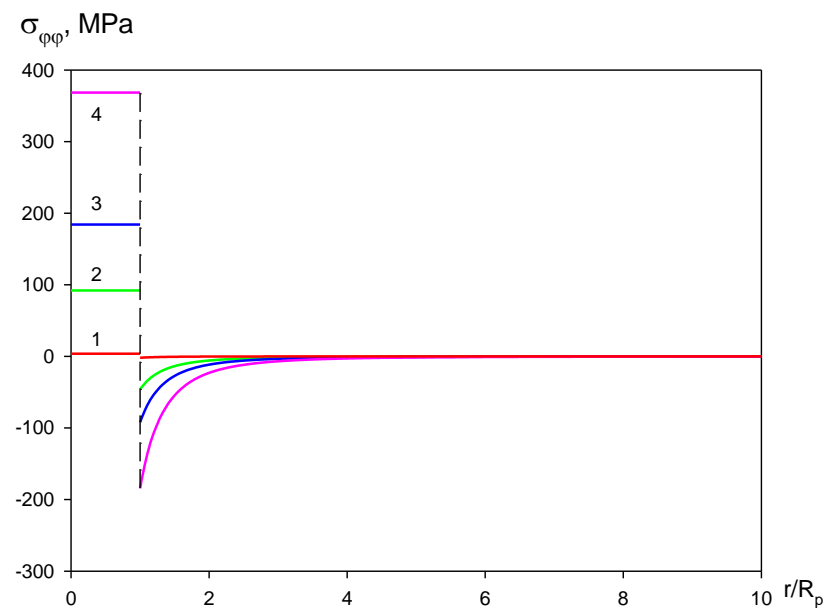


Figure 7. The distribution of the tangential stresses σ_{rr} in the particle and matrix for various values of the temperature difference: 1— $\Delta T = 10$ K; 2—50 K; 3—100 K; 4—200 K.

Note that, due to spherical symmetry, tangential and meridional stresses are equal: $\sigma_{\varphi\varphi} = \sigma_{\theta\theta}$.

An analysis of the effect of the temperature difference ΔT on the stress state allows us to conclude that, with growth, there is an increase in stresses in the particle and the adjacent part of the matrix. In this case, to a first approximation, the magnitude of the arising stresses is proportional to ΔT .

Let us determine the maximum shear stresses $\tau_{\max} = \frac{1}{2} |\sigma_{rr} - \sigma_{\varphi\varphi}|$ arising in a dispersion-strengthened material as a result of the temperature change. Figure 8 shows the dependence of maximal shear stresses on the radial coordinate. In the hardened particle, $\tau_{\max} = 0$. A sharp increase in $\tau_{\max} = 0$ occurs at the interface between the particle and the matrix. Then, as the distance from the particle boundary increases, the value of the maximum shear stresses $\tau_{\max} = 0$ monotonously decreases and becomes vanishingly small.

According to the condition of Saint Venant and Tresca, the plastic deformation begins when the maximal shear stress reaches half of the yield strength. The mathematical formulation of this condition has the following form [52]:

$$\tau_{\max} = \frac{1}{2} \tau_0. \quad (27)$$

It is very critical for an engineer to locate and evaluate the maximum shear stress in a material in order to design the construction in such a way to resist failure.

On the basis of the dependences in Equations (11) and (12), it is possible to determine the magnitude of the temperature difference leading to the occurrence of plastic deformation.

$$\Delta T_{pl} = \frac{3K_p + 4\mu_m}{9K_p\mu_m(\alpha_p - \alpha_m)} \tau_0. \quad (28)$$

According to Equation (22), the plastic deformation due to thermal stresses of the aluminum matrix with strengthening scandium fluoride particles occurs when the temperature difference is approximately equal to 72 K. Therefore, above thermal stress, consideration should be given when designing technological constructions for a considerable temperature range.

Figure 9 shows the dimensionless stress intensity $\tau_* = \tau_{\text{int}}/\tau_{\text{scale}}$ in the vicinity of nine particles. The scale used here is the stress intensity at the particle–matrix interface.

$$\tau_{\text{scale}} = 6\sqrt{3} \frac{K_p \mu_m}{3K_p + 4\mu_m} (\alpha_p - \alpha_m) \Delta T. \quad (29)$$

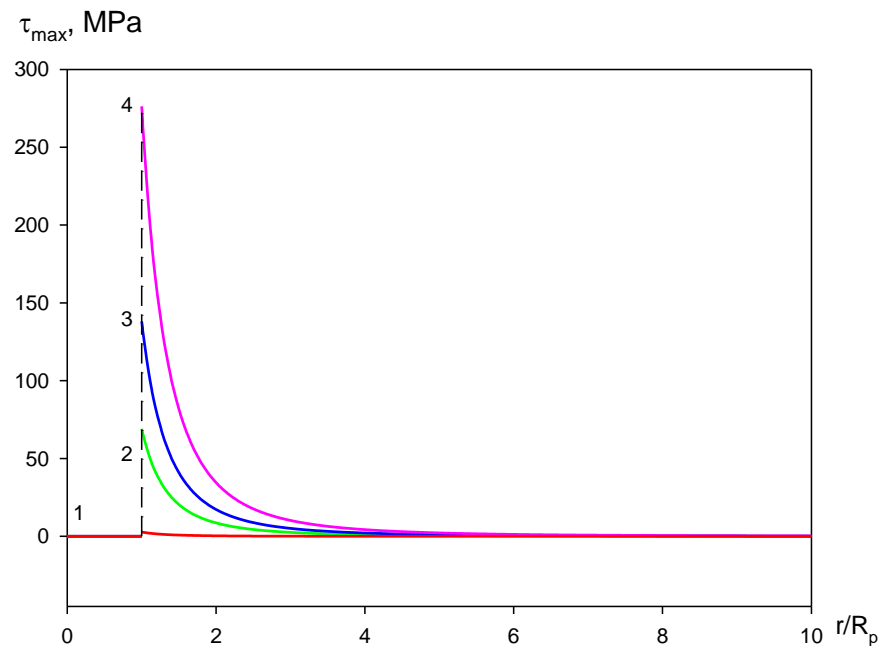


Figure 8. The distribution of the maximal shear stresses σ_{rr} in the particle and matrix for various values of the temperature difference: 1— $\Delta T = 10$ K; 2—50 K; 3—100 K; 4—200 K.

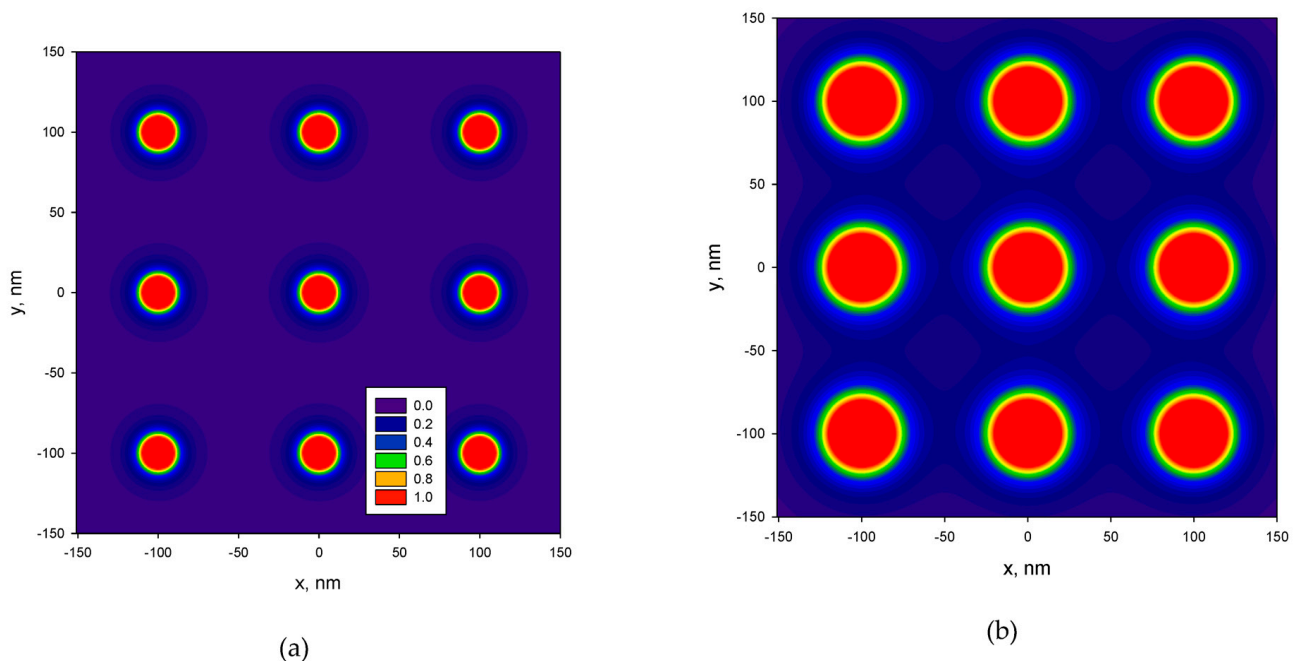


Figure 9. Dimensionless intensity of thermal stresses. Distance between hardening particles $\Lambda_p = 100$ nm: (a) $R_p = 5$ nm; (b) $R_p = 20$ nm.

The highest stress values were observed in particles. With distance from the particles, the stress intensity sharply decreased. With an increase in the size R_p of particles at the same distance between them Λ_p , the region in which thermal stresses were observed caused by the difference in the coefficients of thermal expansion of the matrix and the particle increased. The influence of neighboring particles at $R_p < 0.2\Lambda_p$ was insignificant.

Thus, with a small volume fraction $f = (2R_p/\Lambda_p)^3 < 0.06$, the analysis of the stress–strain state of the dispersion-hardened material caused by the difference in thermal expansion coefficients could be carried out without taking up to the effects of the collective interaction of particles and the matrix.

Figure 10 shows the dependence of σ_{CTE} on the volume fraction of hardening particles, calculated for different values of ΔT .

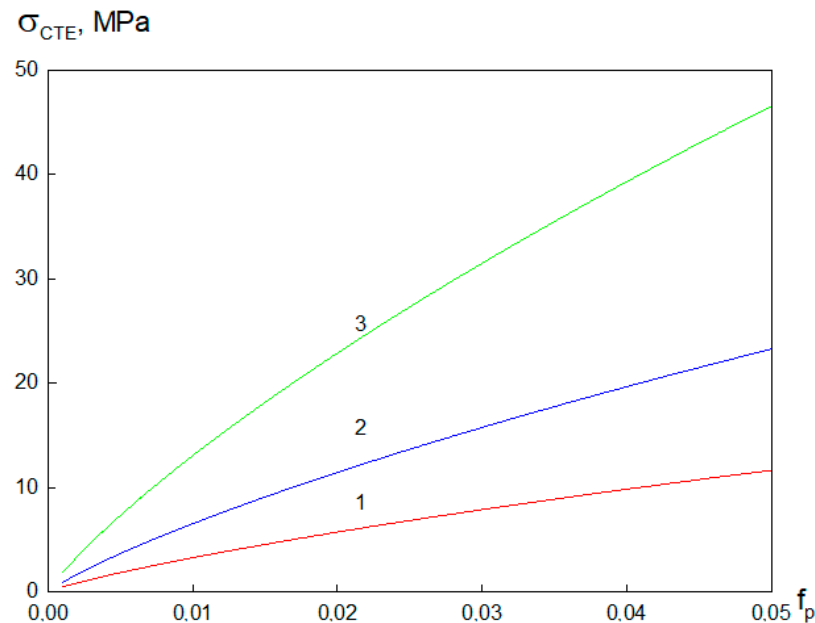


Figure 10. Dependence of thermal stresses σ_{CTE} in the A356 alloy hardened by ScF_3 particles on the volume fraction of hardening particles, calculated for various values of ΔT . Particle size $\delta_p = 80$ nm: 1— $\Delta T = 50$ K; 2— $\Delta T = 100$ K; 3— $\Delta T = 200$ K.

Figure 10 shows that, with an increase in the volume fraction of hardening particles, an increase in thermal stresses occurred σ_{CTE} . This fact was associated with an increase in the number of hardening particles in the alloy and, accordingly, with an increase in their contribution to the hardening of the material. When the material was heated or cooled, as a result of the mismatch between the thermal expansion coefficients and the elastic constants of the matrix and the particles, thermal stresses increased. The calculation results show that an increase in the volume fraction of the strengthening ScF_3 particles in the A356 alloy from 0.1% to 5% at $\Delta T = 50$ K led to an increase in σ_{CTE} from 0.46 MPa to 11.8 MPa, and, at $\Delta T = 200$ K, it led to an increase in σ_{CTE} from 1.84 MPa to 46.538 MPa.

Figure 11 shows the dependence σ_{CTE} on the volume fraction of particles in alloys, hardened by particles from different materials with a temperature change $\Delta T = 100$ K.

The qualitative behavior of all curves in Figure 11 coincides with an increase in the volume fraction of the hardening phase, while an increase in stresses occurs σ_{CTE} . However, the intensity of the stresses depends on the material of the hardening particles. Thus, with a volume fraction $f_p = 5\%$ and a temperature difference $\Delta T = 100$ in alloys hardened with ScF_3 particles, the thermal stresses are $\sigma_{CTE} = 23.61$ MPa; when hardened with Al_2O_3 particles, the magnitude of thermal stresses is $\sigma_{CTE} = 37.64$ MPa; when hardened with TiO_2 , it is $\sigma_{CTE} = 40.53$ MPa. A comparison of calculations performed according to Equation (25) with calculations performed according to Equation (7) shows that, for small volume fractions of the hardening phase, Equation (7) underestimates σ_{CTE} , and, for large values of f_p in predicting σ_{CTE} using Equation (7), one can consider an average estimate for particles of different composition.

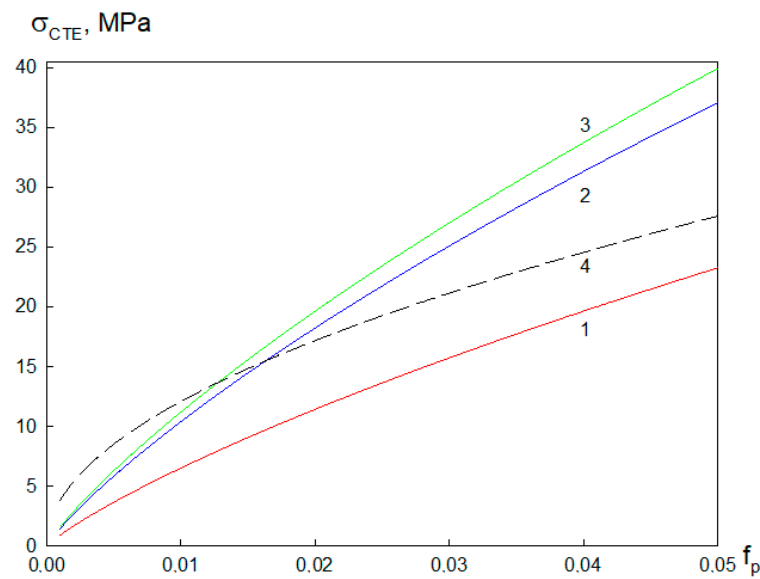


Figure 11. Dependence of thermal stresses σ_{CTE} in the A356 alloy on the volume fraction of hardening particles; particle size $\delta_p = 80$ nm, $\Delta T = 100$ K. Curves 1–3 correspond to the calculation using Equation (25), while curve 4 corresponds to the calculation using Equation (7): 1—ScF₃; 2—TiO₂; 3—Al₂O₃.

The contributions of the described mechanisms to the yield strength of the composite calculated from Equations (3), (4), (6), and (25) are presented in Figure 12. The results demonstrate that theoretical values are very close to the experimental data. The strengthening caused by thermal mismatch makes the largest contribution to the yield strength improvement. The yield strength increments due to Nardon–Prewo and Orowan mechanisms are much lower.

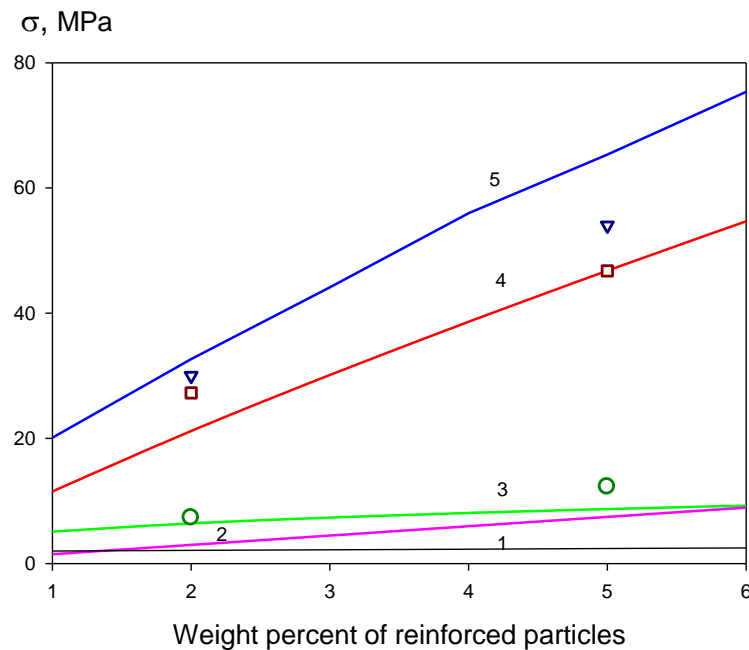


Figure 12. Dependence of different strengthening mechanisms on the mass fraction of the hardening particles: 1—Hall–Petch stresses; 2—Nardon and Prewo stresses; 3—Orowan stresses; 4—thermal stresses; 5—strengthening stresses $\sigma_{Str} = \sigma_{NP} + \sigma_{HP} + \sigma_{Or} + \sigma_{CTE}$; ○—Orowan stresses [53]; □—thermal stresses [53]; ▽—strengthening stresses [53].

The predicted values of the total improvement in yield strength due to various strengthening mechanisms were 31 MPa and 61 MPa for the alloys with 2% and 5% mass fraction of Al_2O_3 . Experimental results [53] showed that the strengthening stresses are equal to 30 MPa and 45 MPa, respectively. The difference between the experimental and theoretical results for the alloy with the 5% mass fraction of Al_2O_3 may be explained by the agglomeration of the hardening particles in the composite.

Figure 13 shows the dependence of the yield strength on the mass fraction of the second phase in alloys reinforced with particles of different materials with a change in temperature $\Delta T = 100$. An increase in the mass fraction of particles led to an increase in the limiting shear stress for all considered cases. The smallest values τ_0 were observed for alloys hardened with titanium oxide. At low values of the mass fraction (less than 2%), the highest values τ_0 were achieved in alloys hardened with scandium fluoride; at large values of the mass fraction of the second phase, the highest values were achieved in alloys hardened with alumina.

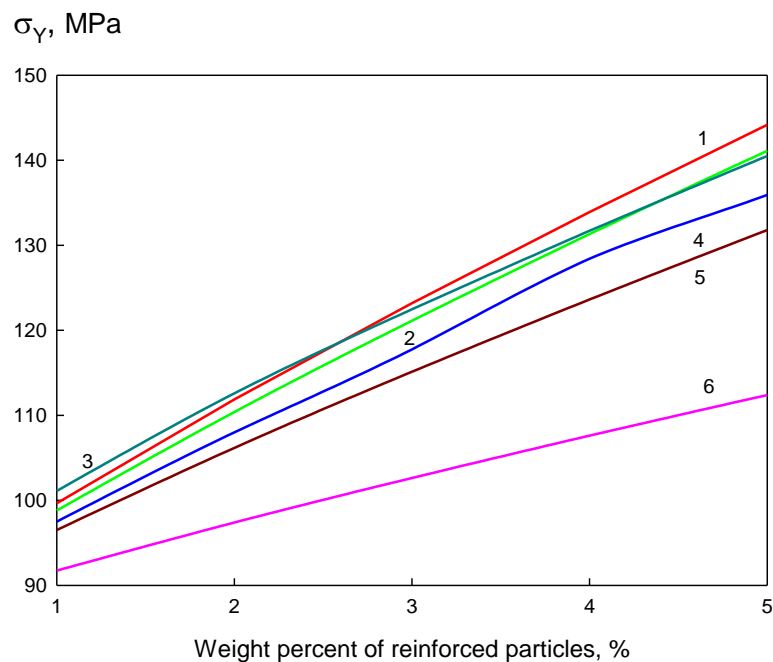


Figure 13. Dependence of the yield stress on the mass fraction of the second phase in alloys strengthened by particles of different materials with temperature difference $\Delta T = 100$ K: 1—SiC; 2 — B_4C ; 3— ScF_3 ; 4— TiB_2 ; 5— Al_2O_3 ; 6— TiO_2 .

3.3. Verification of the Results

Verification of the modeling results was carried out by comparison with experimental data. Table 4 presents the mechanical properties of the A356 alloy and A356-based composites.

Table 4 shows both experimental results and theoretical predictions of the yield strength σ_Y for different temperatures. The yield strength of composites was greatly enhanced with an increase in reinforcement ratio for all tested conditions. A considerable improvement in yield strength of the composite was recorded with integration into the matrix of the 1% Al_2O_3 and 1% ScF_3 disperse phase. The enhancement in strain hardening capacity of a composite at elevated temperature led to decreased variations in the yield strength of composites compared with aluminum alloy A356.

Table 4. Yield strength of A356 alloy and A356-based composites.

Alloy	Room Temperature, $\Delta T = 0$		$\Delta T = 50$ K		$\Delta T = 100$ K	
	σ_Y , MPA, Experiment	σ_Y , MPA, Results of Modeling	σ_Y , MPA, Experiment	σ_Y , MPA, Results of Modeling	σ_Y , MPA, Experiment	σ_Y , MPA, Results of Modeling
A356	85 ± 8	-	74 ± 4	-	61 ± 6	-
A356–1%Al ₂ O ₃	113 ± 6	107	106 ± 5	101	100 ± 6	97
A356–1%ScF ₃	109 ± 8	114	107 ± 4	111	98 ± 6	102

Upon comparing the experimental and theoretical values, one can see that, in general, the results of the predictions were fairly close to the experimental data. The good correlation between the experimental measurements and simulation results validates the correct methods and approaches for the simulation of processes of plastic deformation.

4. Conclusions

An experimental and theoretical investigation of the strength properties of aluminum alloys strengthened by nanoparticles, as well as a determination of the significance of various mechanisms responsible for the strengthening of the material, was carried out.

Results of experimental investigation demonstrated that the hardening of aluminum alloy A356 by Al₂O₃ and ScF₃ nanoparticles led to an increase in the yield strength, ultimate tensile strength, and plasticity. The introduction of 0.2 wt.% Al₂O₃ nanoparticles made it possible to increase the yield strength, ultimate tensile strength, and plasticity from 85 to 100 MPa, from 130 to 180 MPa, and from 3.5% to 4.1%, respectively, and an increase in the content of Al₂O₃ nanoparticles allowed an increase in the yield strength and ultimate tensile strength of the alloy to 113 MPa and 195 MPa, respectively.

The use of 0.2 wt.% ScF₃ nanoparticles increased the yield strength, ultimate tensile strength, and ductility of the A356 aluminum alloy to 98, 190 MPa, and 4.3%, respectively, and an increase in the content of ScF₃ nanoparticles made it possible to increase the yield strength and ultimate tensile strength of the alloy to 109 MPa and 250 MPa, respectively. Despite the similar size of Al₂O₃ and ScF₃ nanoparticles (~80 nm), the physicomechanical properties of nanoparticles significantly affected the possibility of increasing the mechanical properties of the A356 aluminum alloy.

A physicomathematical model of the occurrence of thermal stresses was developed caused by the mismatch of the coefficients of thermal expansion of the matrix and strengthening particles, on the basis of the fundamental principles of mechanics of a deformable solid, and in contrast to existing models, taking into account the elastic properties of not only the matrix, but also the particle.

In the case of thermal deformation of dispersion-hardened alloys, when the CTE of the matrix and particles noticeably differ, an additional stress field is created in the vicinity of the strengthening particle. Thermal stresses increase the effective particle size. This phenomenon can significantly affect the result of the assessment of the yield strength.

In the particle, the stresses are constant. In the matrix material, these stresses decrease quite sharply. As the distance from the particle increases, the value of the shear stresses monotonously decreases and becomes vanishingly small, when the distance from the particle boundary exceeds five particle diameters.

The growth of temperature difference leads to an increase in contact pressure between the matrix and the particle. On the inner surface of the matrix, plastic flow begins when the maximum shear stresses exceed the yield strength of the material at a given temperature. The plastic deformation due to thermal stresses of the aluminum matrix with strengthening scandium fluoride particles occurs when the temperature difference is equal to approximately 72 K.

The strengthening caused by thermal mismatch makes the largest contribution to the yield strength improvement. The yield strength increments due to Nardon–Prewo and Orowan mechanisms are much lower.

Author Contributions: Conceptualization, O.M., O.D. and A.K.; methodology, O.M. and I.Z.; software, O.M.; validation, O.D. and T.K.; formal analysis, O.D. and T.K.; investigation, O.D. and A.K.; writing, O.M. and O.D.; supervision and funding acquisition, A.V. All authors read and agreed to the published version of the manuscript.

Funding: This work was financially supported by Grant N 17-13-01252 from the Russian Science Foundation and Ministry of Science and Higher Education of the Russian Federation, project No 0721-2020-0028.

Data Availability Statement: The data presented in this study are available in the article.

Acknowledgments: The authors acknowledge the Russian Science Foundation under Grant N 17-13-01252. I.Z. and A.K. acknowledge the financials support by the Ministry of Science and Higher Education of the Russian Federation, project No 0721-2020-0028.

Conflicts of Interest: The authors declare no conflict of interest.

References

1. Chawla, N.; Chawla, K.K. *Metal Matrix Composites*; Springer: New York, NY, USA, 2006; 211p, eBook ISBN 978-0-387-28567-2, Hardcover ISBN 978-0-387-23306-2, Softcover ISBN 978-1-4614-9843-8. [[CrossRef](#)]
2. Natarajan, N.; Vijayarangan, S.; Rajendran, I. Wear behaviour of A356/25SiCp aluminium matrix composites sliding against automobile friction material. *Wear* **2006**, *261*, 812–822. [[CrossRef](#)]
3. Weinert, K.; Lange, M.; Schoer, M. Machining of Light-metal Matrix Composites. In Proceedings of the 6th International Conference Magnesium Alloys and Their Applications, Frankfurt, Germany, 20 September 2000; ISBN 3-527-30282-4. [[CrossRef](#)]
4. Karabasov, Y.S. *Advanced Materials*; MISIS: Moscow, Russia, 2002; 736p.
5. Ashby, M.F.; Johnson, K. *Materials and Design, the Art and Science of Materials Selection in Product Design*; Butterworth Heinemann: Oxford, UK, 2002; 602p, ISBN 0750655542/978-0750655545.
6. Arnhold, V.; Hummert, K. *New Materials by Mechanical Alloying Techniques*; Arzt, E., Schult, L., Eds.; DGM Informationsgesellschaft Verlag: Oberursel, Germany, 1989; 263p, ISBN 3-88355-133-3.
7. Orowan, E. Discussion on internal stresses. In *Symposium on Internal Stresses in Metals and Alloys*; Institute of Metals: London, UK, 1948; pp. 451–453.
8. Ashby, M.F. Work hardening of dispersion-hardened crystals. *Philos. Mag.* **1966**, *14*, 1157–1178. [[CrossRef](#)]
9. Hirsch, P.B.; Humphreys, F.J. Comment on “Dispersion hardening in metals” by E.W. Hart. *Scr. Metall.* **1973**, *7*, 259–267. [[CrossRef](#)]
10. Hazzledine, P.M.; Hirsch, P.B. A coplanar Orowan loops model for dispersion hardening. *Philos. Mag.* **1974**, *30*, 1331–1351. [[CrossRef](#)]
11. Humphreys, F.J.; Hirsch, P.B. Work-hardening and recovery of dispersion hardened alloys. *Philos. Mag.* **1976**, *34*, 373–390. [[CrossRef](#)]
12. Hansen, N. Dispersion strengthening of aluminium-aluminium-oxide products. *Acta Met.* **1970**, *18*, 137–145. [[CrossRef](#)]
13. Spigarelli, S.; Paoletti, C. A new model for the description of creep behaviour of aluminium-based composites reinforced with nanosized particles. *App. Sci. Manuf.* **2018**, *112*, 346–355. [[CrossRef](#)]
14. Kröpfl, I.; Vöhringer, O.; Macherauch, E. Creep Behavior of Dispersion-Hardened Aluminum Materials. *Mechan. Time Depend. Mater.* **1999**, *3*, 1–13. [[CrossRef](#)]
15. Stobrawa, P.; Rdzawski, Z.M.; Głuchowski, W. Structure and properties of dispersion hardened submicron grained copper. *J. Achiev. Mater. Manufact. Eng.* **2007**, *20*, 195–198.
16. Novikov, N.V.; Bogatyreva, G.P.; Bogdanov, R.K.; Il’nitskaya, G.D.; Isonkin, M.; Marinich, M.A.; Tkach, V.N.; Tsysar’, M.A.; Zaitseva, N. The effect of the additions of nanodispersed diamonds on physico-mechanical properties of the drilling tool metal matrix. *J. Superhard Mater.* **2011**, *33*, 268–273. [[CrossRef](#)]
17. Chen, B.; Shen, J.; Ye, X.; Jia, L.; Li, S.; Umeda, J.; Takahashi, M.; Kondoh, K. Length effect of carbon nanotubes on the strengthening mechanisms in metal matrix composites. *Acta Mater.* **2017**, *140*, 317–325. [[CrossRef](#)]
18. Zhou, W.; Yamaguchi, T.; Kikuchi, K.; Nomura, N.; Kawasaki, A. Effectively enhanced load transfer by interfacial reactions in multi-walled carbon nanotube reinforced Al matrix composites. *Acta Mater.* **2017**, *125*, 369–376. [[CrossRef](#)]
19. Cao, G.; Chen, X.; Kysar, J.W.; Lee, D.; Gan, Y.X. The mean free path of dislocations in nanoparticle and nanorod reinforced metal composites and implication for strengthening mechanisms. *Mech. Res. Commun.* **2007**, *34*, 275–282. [[CrossRef](#)]
20. Daneyko, O.I.; Kovalevskaya, T.A.; Matvienko, O.V. The influence of incoherent nanoparticles on thermal stability of aluminum alloys. *Russ. Phys. J.* **2018**, *61*, 1229–1235. [[CrossRef](#)]
21. Daneyko, O.I.; Kovalevskaya, T.A.; Kulaeva, N.A. Modeling of plastic deformation of dispersion-hardened materials with L1₂ superstructure particles. *Russ. Phys. J.* **2017**, *60*, 508–514. [[CrossRef](#)]
22. Daneyko, O.I.; Kovalevskaya, T.A. Temperature effect on stress-strain properties of dispersion-hardened crystalline materials with incoherent nanoparticles. *Russ. Phys. J.* **2019**, *61*, 1687–1694. [[CrossRef](#)]
23. Kovalevskaya, T.A.; Daneyko, O.I. The influence of scale parameters of strengthening phase on plastic shear zone in heterophase alloys with incoherent nanoparticles. *Russ. Phys. J.* **2020**, *62*, 2247–2254. [[CrossRef](#)]

24. Matvienko, O.; Daneyko, O.; Kovalevskaya, T. Mathematical modeling of plastic deformation of a tube from dispersion-hardened aluminum alloy. *MATEC Web Conf.* **2018**, *243*, 8. [[CrossRef](#)]
25. Matvienko, O.V.; Daneyko, O.I.; Kovalevskaya, T.A. Elastoplastic deformation of dispersion-hardened aluminum tube under external pressure. *Russ. Phys. J.* **2018**, *61*, 1520–1528. [[CrossRef](#)]
26. Matvienko, O.V.; Daneyko, O.I.; Kovalevskaya, T.A. Elastoplastic deformation of dispersion-hardened aluminum tube under external and internal pressure. *Russ. Phys. J.* **2019**, *62*, 720–728. [[CrossRef](#)]
27. Huang, Y.D.; Hort, N.; Dieringa, H.; Kainer, K.U. Analysis of instantaneous thermal expansion coefficient curve during thermal cycling in short fiber reinforced AlSi12CuMgNi composites. *Compos. Sci. Technol.* **2005**, *65*, 137–147. [[CrossRef](#)]
28. Vaidya, R.U.; Chawla, K.K. Thermal expansion of metal–matrix composites. *Comp. Sci. Technol* **1994**, *50*, 13–22. [[CrossRef](#)]
29. Arsenaault, R.J.; Shi, N. Dislocations generation due to differences between the coefficients of thermal expansion. *Mater. Sci. Eng.* **1986**, *81*, 151–187. [[CrossRef](#)]
30. Lee, J.K.; Earmme, Y.Y.; Aaronson, H.I.; Russell, K.C. Plastic relaxation of the transformation strain energy of a misfitting spherical precipitate: Ideal plastic behavior. *Metall. Mater. Trans. A* **1980**, *11*, 1837–1847. [[CrossRef](#)]
31. Yang, C.; Sun, W.; Seneviratne, W.; Shashidhar, A. Thermally induced loads of fastened hybrid composite/aluminum structures. *J. Aircr.* **2008**, *45*, 569–580. [[CrossRef](#)]
32. Parrini, L.; Schaller, R. Thermal stresses in metal matrix composites studied by internal friction. *Acta Mater.* **1996**, *44*, 4881–4888. [[CrossRef](#)]
33. Drozd, Z.; Trojanová, Z.; Lukáč, P. Temperature deformation of the ax41 composites studied by the dilatometer measurements. In Proceedings of the ECCM15—15th European Conference on Composite Materials, Venice, Italy, 24–28 June 2012; pp. 1–8.
34. Vogelsang, M.; Arsenaault, R.J.; Fisher, R.M. An in situ HVEM study of dislocation generation at Al/SiC interfaces in metal matrix composites. *Metall. Mater. Trans. A* **1986**, *17*, 379–389. [[CrossRef](#)]
35. Dunand, D.C.; Mortensen, A. On plastic relaxation of thermal stresses in reinforced metals. *Acta Metall. Mater.* **1991**, *39*, 127–139. [[CrossRef](#)]
36. Taylor, A.; Jones, R.M. *Silicon Carbide*; O'Connor, J.R., Smiltens, J., Eds.; Pergamon: Oxford, UK, 1960; pp. 147–154.
37. Chowdhury, A.S.M.F.; Mari, D.; Schaller, R. Thermal stress relaxation in magnesium matrix composites studied by mechanical spectroscopy. *Phys. Stat. Sol.* **2008**, *205*, 249–254. [[CrossRef](#)]
38. Brinker, C.J.; Scherer, G.W. *Sol-Gel Science*; Academic Press: New York, NY, USA, 1990; 881p.
39. Vorozhtsov, S.A.; Eskin, D.G.; Tamayo, J.; Vorozhtsov, A.B.; Promakhov, V.V.; Averin, A.A.; Khrustalyov, A.P. The application of external fields to the manufacturing of novel dense composite master alloys and aluminum-based nanocomposites. *Metall. Mater. Trans. A* **2015**, *46*, 2870–2875. [[CrossRef](#)]
40. Puga, H.; Costa, S.; Barbosa, J.; Ribeiro, S.; Prokic, M. Influence of ultrasonic melttreatment on microstructure and mechanical properties of AlSi9Cu3 alloy. *J. Mater. Process. Technol.* **2011**, *211*, 1729–1735. [[CrossRef](#)]
41. Bisht, A.; Srivastava, M.; Manoj Kumar, R.; Lahir, I.; Lahiri, D. Strengthening mechanism in grapheme nanoplatelets reinforced aluminum composite fabricated through spark plasma sintering. *Mater. Sci. Eng. A* **2017**, *695*, 20–28. [[CrossRef](#)]
42. Nardone, V.C.; Prewo, K.M. On the strength of discontinuous silicon carbide reinforced aluminum composites. *Scr. Metall.* **1986**, *20*, 43–48. [[CrossRef](#)]
43. Yu, H.; Xin, Y.; Wang, M.; Liu, Q. Hall-Petch relationship in Mg alloys: A review. *J. Mater. Sci. Tech.* **2018**, *34*, 248–256. [[CrossRef](#)]
44. Goh, C.; Wei, J.; Lee, L.C.; Gupta, M. Properties and deformation behaviour of Mg–Y₂O₃ nanocomposites. *Acta Mater.* **2007**, *55*, 5115–5121. [[CrossRef](#)]
45. Neite, G.; Kubota, K.; Higashi, K.; Hehmann, F. Magnesium. *Mater. Sci. Tech.* **2005**, *8*, 115.
46. Sanaty-Zadeh, A. Comparison between current models for the strength of particulate-reinforced et al matrix nanocomposites with emphasis on consideration of Hall–Petch effect. *Mater. Sci. Eng. A* **2012**, *531*, 112–118. [[CrossRef](#)]
47. Ma, F.C.; Zhou, J.J.; Liu, P.; Li, W.; Liu, X.K.; Pan, D.; Lu, W.J.; Zhang, D.; Wu, L.Z.; Wei, X.Q. Strengthening effects of TiC particles and microstructure refinement in insitu TiC-reinforced Ti matrix composites. *Mater. Charact.* **2017**, *127*, 27–34. [[CrossRef](#)]
48. Sree Manu, K.M.; Arun Kumar, S.; Rajan, T.P.D.; Riyas Mohammed, M.; Pai, B.C. Effect of alumina nanoparticle on strengthening of Al-Si alloy through dendrite refinement, interfacial bonding and dislocation bowing. *J. Alloys Compd.* **2017**, *712*, 394–405. [[CrossRef](#)]
49. Li, J.; Liu, B.; Fang, Q.H.; Huang, Z.W.; Liu, Y.W. Atomic-scale strengthening mechanism of dislocation-obstacle interaction in silicon carbide particle- reinforced copper matrix nanocomposites. *Ceram. Int.* **2017**, *43*, 3839–3846. [[CrossRef](#)]
50. Zhao, X.; Lu, C.; Tieu, A.K.; Pei, L.Q.; Zhang, L.; Cheng, K.Y.; Huang, M.H. Strengthening mechanisms and dislocation processes in <111> textured nanotwinned copper. *Mater. Sci. Eng. A* **2016**, *676*, 474–486. [[CrossRef](#)]
51. Ma, K.; Lavernia, E.J.; Schoenung, J.M. Particulate reinforced aluminum alloy matrix composites—A review on the effect of microconstituent. *Rev. Adv. Mater. Sci.* **2017**, *48*, 91–104.
52. Timoshenko, S.P.; Goodier, J.N. *Theory of Elasticity*; McGraw Hill: New York, NY, USA, 2010; 567p.
53. Ma, P.; Jia, Y.; Prashanth, K.; Yu, Z.; Yang, S.; Zhao, J.; Li, C. Effect of Al₂O₃ Nanoparticles as Reinforcement on the Tensile Behavior of Al-12Si Composites. *Metals* **2017**, *7*, 359. [[CrossRef](#)]